Evidence of Long-lived Powerful Gyrosynchrotron Radio Emission in the Close Binary FF UMa

The Astrophysical Journal, 1001:112 (9pp), 2026 April 10 https://doi.org/10.3847/1538-4357/ae5629

Evidence of Long-lived Powerful Gyrosynchrotron Radio Emission in the Close Binary FF UMa

Ruijie Gao[1], Jun Yang[2], Yang Gao[3], Jingdong Zhang[4,5], Bo Zhang[4], Wen Chen[6], Xiaohui Sun[1], Guannan Gao[6,7], Zhibin Dai[6,8], and Tobia D. Carozzi[2]
[1] School of Physics and Astronomy, Yunnan University, Kunming 650091, People's Republic of China; ruijiegz@gmail.com, xhsun@ynu.edu.cn
[2] Department of Space, Earth and Environment, Chalmers University of Technology, Onsala Space Observatory, 43992, Onsala, Sweden; jun.yang@chalmers.se
[3] School of Physics and Astronomy, Sun Yat-Sen University, Zhuhai 519082, Guangdong, People's Republic of China
[4] Shanghai Astronomical Observatory, Chinese Academy of Sciences, 80 Nandan Road, Shanghai, People's Republic of China
[5] Department of Geodesy and Geodynamics, Finnish Geospatial Research Institute (FGI), National Land Survey of Finland, Vuorimiehentie 5, Espoo 02150, Finland
[6] Yunnan Observatories, Chinese Academy of Sciences, Kunming 650216, Yunnan, People's Republic of China
[7] Yunnan Key Laboratory of the Solar Physics and Space Science, Kunming 650216, People's Republic of China
[8] Key Laboratory for the Structure and Evolution of Celestial Objects, Chinese Academy of Sciences, Kunming 650216, People's Republic of China
Received 2026 February 15; revised 2026 March 12; accepted 2026 March 20; published 2026 April 8

Abstract

RS Canum Venaticorum (RS CVn) close binaries, characterized by tidal locking, rapid rotations, and strong magnetic fields, are ideal laboratories for high-resolution radio observations to probe emission processes, magnetic field configurations, and interaction activity. Despite their importance, only a few RSCVn sources have been explored by polarimetric observations of very long baseline interferometry. To expand the effort, we have analyzed the existing Very Long Baseline Array (VLBA) astrometric data for the RS CVn binary FF Ursae Majoris. In the 5 GHz VLBA experiments conducted between 2021 and 2024, both total intensity and circularly polarized emission were clearly detected at six of seven epochs. The consistently high brightness temperatures ($\geqslant 10^7$ K) and the moderate fractional circular polarization (10%–30%) over about 3 yr indicate that the radio emission is mainly produced by gyrosynchrotron radiation from mildly relativistic electrons in the highly ordered magnetic field. The radio luminosities are also comparable to those of previously studied powerful RS CVn binaries and show a significant anticorrelation with fractional circular polarization. A mean centroid offset of $13.4 \pm 3.1\,R_{\odot}$ between the Stokes I and V emission was found across multiple epochs, indicating a possible additional contribution from the secondary star via a magnetically active corona, a giant magnetic loop, or significant interaction activity with the primary star in the quiescent state.

Unified Astronomy Thesaurus concepts: Radio continuum emission (1340); Binary stars (154); Stellar magnetic fields (1610); Very long baseline interferometry (1769)

1. Introduction

RS Canum Venaticorum (RS CVn) binary systems are close binaries consisting of a subgiant or giant star of spectral type F, G, or K and a cooler main-sequence companion (D. S. Hall 1981). Because of their strong magnetic activity, these systems are important targets for exploring stellar astrophysics. The short orbital period (1–30 days) leads to tidal synchronization and thus rapid rotation of both stellar components. Combined with their deep convective envelopes, this rapid rotation drives strong magnetic dynamos that power intense chromospheric and coronal activity (T. R. Ayres & J. L. Linsky 1980). Therefore, RS CVn systems can be detected across a wide range of wavelengths, from radio to high-energy bands. As such, RS CVn stars are often regarded as natural laboratories for high-resolution imaging observations to study stellar magnetic field structures and activities.

RS CVn systems have been extensively observed in the radio band since the late 1970s (S. R. Spangler 1977; R. L. Mutel & J. F. Lestrade 1985; D. H. Morris & R. L. Mutel 1988; S. A. Drake et al. 1989). These active binaries produce radio emission through magnetically driven nonthermal processes in their active stellar coronae. The dominant mechanism at the GHz frequency range is likely incoherent gyrosynchrotron radiation from mildly relativistic electrons spiraling in magnetic fields of tens to hundreds of Gauss (G. A. Dulk 1985; M. Güdel 2002; T. Murphy & D. L. Kaplan 2026). This explains the nonthermal radio spectra and significant variability. To date, most observations have been conducted with single-dish telescopes or low-resolution interferometers, limiting our ability to resolve the spatial structure of the emission regions and the magnetic fields (L. D. Matthews 2025). Just a few RS CVn binaries have been observed using very long baseline interferometry (VLBI), with notable examples including UX Ari, HR 1099, and AR Lac (e.g., R. L. Mutel & J. F. Lestrade 1985; R. L. Mutel et al. 1987; M. Massi et al. 1988; W. Chen & M. Wang 2023). High-resolution VLBI studies have revealed complex morphologies in total intensity and circularly polarized emission across multiple wavelengths, providing crucial insights into the geometry of magnetically active regions.

The dominant stellar component responsible for radio emission in RS CVn binaries remains uncertain. Radio emission in these systems is often assumed to be dominated by the primary star, owing to its stronger magnetic activity (A. S. Brun & M. K. Browning 2017) in the corona and the presence of potential giant magnetic loops. HR 1099, being the closest RS CVn binary to Earth, has become the best-studied system in terms of long-term, multiepoch VLBI

Table 1
Orbital Parameters of FF UMa

Parameter	Symbol and Value	References
Spectral type	K1IV + K0V	(1)
Primary radius	$r_{\rm P} = 2.95 R_{\odot}$	(2)
Secondary radius	$r_{\rm S} = 2.30 R_{\odot}$	(2)
Parallax	$\pi = 9.57$ mas	(3)
Eccentricity	$e = 0.0$	(1)
Mass ratio	$q = 2.12 \pm 0.10$	(1)
Orbital inclination	$i_{\rm obs} = 50.^{\circ}5$	(2)
Orbital period	$P = 3.27487 \pm 0.00004$ days	(2)
Ephemeris epoch (MJD)	$T_{\rm eph} = 54067.019 \pm 0.0017$	(2)

Note. Reference.(1) M. C. Gálvez et al. (2007); (2) H. V. Şenavcı et al. (2020); (3) K. G. Strassmeier et al. (2012).

observations (e.g., J. F. Lestrade et al. 1984; R. L. Mutel et al. 1984, 1985; M. Massi et al. 1988). With the advent of the Very Long Baseline Array (VLBA), R. R. Ransom et al. (2002) obtained high-resolution 8.4 GHz images, resolving a double-peaked radio structure during a flaring state and providing evidence that the radio-emitting regions corotate with the binary on timescales of hours. More recently, W. W. Golay et al. (2024) conducted multiepoch VLBA astrometric observations and found that the radio emission centroid of HR 1099 is systematically offset from the binary center of mass at all observed epochs, with its positional behavior indicating that the radio emission is predominantly associated with the primary star.

In some RS CVn systems, both stellar components may contribute to the radio emission. For example, R. L. Mutel et al. (1985) reported that UX Ari exhibits a characteristic core–halo radio morphology, with the compact core associated with the primary star and the extended halo linked to the secondary star. In later VLBI observations of UX Ari, however, the giant halo was not detected (e.g., W. M. Peterson et al. 2011).

A different case suggests that the secondary star may dominate the radio emission. Using multiepoch VLBA observations at 15 GHz, E. Abbuhl et al. (2015) carried out phase-referenced radio astrometry of the RS CVn binary system HR 5110. After accounting for proper motion, parallax, and orbital motion, they found that the radio emission centroid is consistently coincident with the K-type secondary star. This result supports an interpretation in which the radio emission in HR 5110 is dominated by the K-type subgiant secondary component rather than the F-type subgiant primary star or an interbinary interaction region. To date, long-term VLBI detections of both stellar components have not been reported in RS CVn binaries.

Among known RS CVn systems, FF Ursae Majoris (FF UMa; also known as 2RE J0933+624 or HD 82286) stands out as a particularly active binary that has received some prior study. Because of significant chromospheric activity discovered in the ROSAT EUV all-sky survey by K. A. Pounds et al. (1993), it was classified as a close binary with a period of ∼3.27 days (R. D. Jeffries et al. 1995; R. F. Griffin 2012). The accurate orbital parameters of FF UMa are summarized in Table 1. As a rapidly rotating and tidally locked binary, both stellar components show rarely seen strong Hα emission and photometric variability, indicating extraordinary magnetic activity (K. Strassmeier et al. 2000; M. C. Gálvez et al. 2007; H. V. Şenavcı et al. 2020). FF UMa has also been detected in several wide-field radio surveys, including the LOFAR Two-meter Sky Survey (T. W. Shimwell et al. 2017), the Faint Images of the Radio Sky at Twenty Centimeters survey (R. H. Becker et al. 1995), the National Radio Astronomy Observatory (NRAO) Very Large Array (VLA) Sky Survey (J. J. Condon et al. 1998), and the VLA Sky Survey (M. Lacy et al. 2020). However, these radio observations were obtained with limited angular resolution and at sparse epochs, leaving the spatial origin and geometry of the radio emission largely unconstrained. High-resolution, multi-frequency VLBI observations are therefore essential to investigate the spatial distribution of the radio emission, to identify the dominant radiation mechanisms at GHz frequencies, and to constrain the geometry and strength of the magnetic fields in FF UMa.

In this study, we reanalyzed the existing VLBA data of FF UMa. By combining these data with the well-constrained orbital and rotational parameters of the system, we determined the degree and handedness of polarization, assessed the underlying emission mechanisms, and investigated the spatial structure of the binary's magnetic field. Section 2 describes the observations and data processing; Section 3 presents our results; Section 4 discusses these findings; and Section 5 concludes the paper.

2. VLBA Observations and Data Reduction

FF UMa was observed with the VLBA in 2021 and 2024 under the VLBA project codes BZ087 (PI: Bo Zhang), BZ103 (PI: Jingdong Zhang), and BZ107 (PI: Jingdong Zhang) at 4.8 GHz. These projects were mainly designed to validate the Gaia Celestial Reference Frame via VLBI astrometry (W. Chen et al. 2023; J. Zhang et al. 2024, 2025, 2026).

Because these experiments were performed in the phase-referencing mode (cycle observations of FF UMa and nearby calibrators), their data could also allow us to search for highly circular polarized emission from the weak radio star FF UMa without the standard calibration of small (about a few percent) instrumental cross-polarization leakages (e.g., D. C. Homan & J. F. C. Wardle 1999). In total, seven epochs were observed; the date and participating antennas for each epoch are listed in Table 2. Each epoch included 9–10 VLBA antennas, recording at 4096 Mbps (four intermediate frequencies, IFs, in dual circular polarization, each 128 MHz wide, with two-bit quantization). FF UMa was observed for ∼40–45 minutes epoch^{-1}, with a phase-referencing cycle time of 4 minutes. The raw data were correlated with the VLBA DiFX software correlator (A. T. Deller et al. 2007) using 2 s integration and 0.5 MHz frequency resolution.

The original observations were designed following the MultiView strategy (M. J. Rioja et al. 2017; J. Zhang et al. 2026). Given the small angular separation between FF UMa and the calibrator J0921+6215 (from the ICRF3 catalog), the phase solutions derived from this source sufficiently capture atmospheric effects, making the data reduction effectively equivalent to standard phase referencing. J. Zhang et al. (2026) compared calibration using this single phase calibrator with the MultiView approach and found that the resulting astrometric uncertainties are at a comparable level. During the observations, this phase calibrator had an average flux density of ∼0.46 Jy.

Table 2
Dates and Participating Antennas of the VLBA Observations

Epoch	Project Code	Date (yyyy-mm-dd)	MJD (mid-epoch)	Phase	Absent Stations	Beam Maj(mas)	Beam Min(mas)	Beam PA(deg)
(1)	(2)	(3)	(4)	(5)	(6)	(7)	(8)	(9)
1	BZ087D1	2021-10-09	59496.6745	0.128	PT	3.65	1.22	6.86
2	BZ087D2	2021-12-06	59554.5161	0.791	MK	3.25	1.68	−7.03
3	BZ103D1	2024-04-14	60414.1626	0.289	⋯	2.69	1.17	−7.93
4	BZ103D2	2024-05-06	60436.0896	0.984	FD	2.88	1.14	−0.35
5	BZ103D3	2024-06-05	60466.0206	0.124	⋯	2.76	1.18	−7.65
6	BZ107D1	2024-10-18	60601.6493	0.539	⋯	2.81	1.23	−11.72
7	BZ107D2	2024-12-07	60651.5125	0.765	⋯	2.84	1.24	−11.23

Note. Column (6) lists the VLBA stations that did not participate in each observing epoch. The VLBA stations are Brewster, Fort Davis (FD), Hancock, Kitt Peak, Los Alamos, Maunakea (MK), North Liberty, Owens Valley, Pie Town (PT), and Saint Croix. Columns (7)–(9) give the major axis, minor axis, and position angle of the CLEAN restoring beam used in the final VLBA images, which are also shown in the lower-left corner of each panel in Figure 1.

Visibility data were calibrated and imaged using the NRAO software package Astronomical Image Processing System (AIPS; E. W. Greisen 2003). The calibration steps followed this sequence: First, we did minor amplitude corrections in cross-correlation data due to errors in sampler thresholds using measurements of autocorrelation data. Second, system temperature data and antenna gain curves were used to perform a priori amplitude calibration. Third, the phase errors resulting from the changes in the parallactic angle were corrected. Fourth, the Earth orientation parameters (EOPs) were updated according to the EOP products provided by the United States Naval Observatory, and the related phase errors were corrected. Fifth, the dispersive delays due to the propagation effect in the Earth ionosphere were derived and removed with the global total electron content maps provided by the Global Navigation Satellite System community. Sixth, the AIPS task FRING was first applied to the bright calibrator B0217+734 for manual phase calibration. After applying these solutions, we combined all IFs and both Stokes *RR* and *LL* to perform a global fringe fitting on the phase-referencing calibrator J0921+6215. To gain accurate phase interpolations from calibrator to target scans, we smoothed fringe rate solutions. Finally, we applied the accumulated complex gain solutions and split the data into single-source files. We did deconvolution and self-calibration on the phase-referencing calibrator with the AIPS tasks IMAGR and CALIB. The calibrator shows a core–jet structure with a bright core and a faint, tail-like, short jet toward the northwest. According to the nonthermal synchrotron emission mechanism and statistical research on radio sources (e.g., D. C. Homan & M. L. Lister 2006), its circular polarization fraction is expected to be very low (<1%) and can be safely used as a zero-*V* calibrator for self-calibration. Using the final source model, we also reran self-calibration with the multisource data file and then transferred both amplitude and phase solutions to the target source. After applying the final solutions, we imaged FF UMa with the default Briggs robust weighting parameter of zero and without any self-calibration.

3. Detections of Stokes *I* and *V* Emission in Magnetically Active Binary FF Uma

The target RS CVn binary FF UMa was clearly detected with a signal-to-noise ratio (SNR) of 14–18 in all epochs, as shown in Figure 1. Table 3 summarizes the imaging results of Stokes *I* and *V*. Their total flux densities (S_I, S_V), ratios ($f_c = \frac{|S_V|}{S_I}$), and positional offsets are also shown in Figures 2 and 3. These results were derived through fitting an elliptical Gaussian model to the Stokes *I* and *V* maps using the AIPS task JMFIT. The fitted parameters include the source peak brightness, integrated flux density, position, major and minor axis sizes, and the position angle of the major axis. The VLBA observations covered a broad range of orbital phases and had a relatively uniform distribution (see Figure 2). The maximum gap is approximately 0.2 phase between adjacent epochs.

FF UMa displays significant variability between epochs in Figure 2. It might be in the flare state with significantly high flux densities (10.94 ± 0.67 and 33.37 ± 1.90 mJy) in epochs 3 and 6 and in the quiescent state with relatively low and stable flux densities (1.94–3.07 mJy). Significant circular polarization emission was also detected in six of seven epochs. All detected Stokes *V* components show left-handed helicity and relatively stable total flux densities, 0.32–0.76 mJy. Due to nondetection of Stokes *V* emission in epoch 3, only $\pm 3\sigma$ limits were given. To verify the reliability of the calibration, we also examined the imaging results of the compact calibrator J0921+6215. Its total flux density remained relatively stable, varying by less than 10% across all epochs. No signal exceeding 3σ in the on-source region was detected in the Stokes *V* maps (e.g., Figure 5 in Appendix A). For all seven epochs, these values are very small ($\leqslant$1.2%), supporting the conclusion that the flux density variations and large fractional circular polarization (10%–30%) observed in FF UMa are intrinsic to the target source. Uncorrected cross-polarization leakage can convert a fraction of the linear polarization into a spurious circular polarization signal in the data. According to the early investigation by D. C. Homan & J. F. C. Wardle (1999), this spurious signal is small (<0.25%), even if we assume an unusually high fractional linear polarization of 10% (e.g., R. L. Mutel et al. 1984; R. B. Phillips et al. 1996; D. M. Salter et al. 2010). Its impact on the position measurements is therefore not significant ($<1\sigma$) in the Stokes *V* maps.

The physical emission regions of *I* and *V* are intrinsically extended and overlapping. The minor offsets between their centroids could help us to reveal a hint for the nonuniform distribution of the circular polarization degree in the sky plane. In Figure 3(a), the offsets between the Stokes *I* and *V* centroids show a relatively random distribution. To remove the potential impact of the orbital motion across epochs, we took the position angle from the main to the secondary stars as the reference direction in each epoch and made another plot in

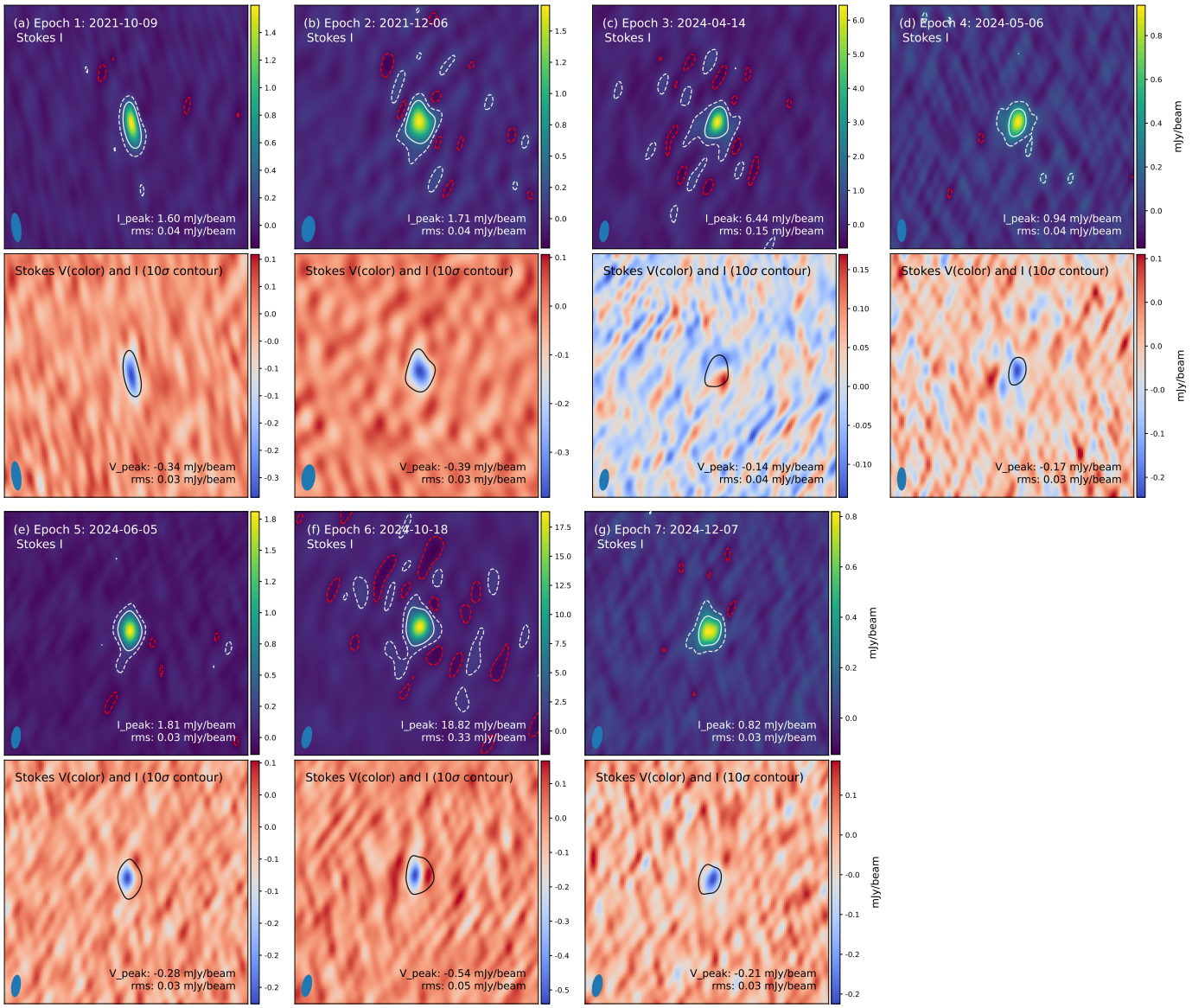

Figure 1. Images of the target source FF UMa in all epochs. Each panel covers a field of view of 30 × 30 mas^2. The color bar on the right side of each panel is in units of mJy/beam^{-1}. In each panel, the upper subpanel shows the Stokes I image and its $+10\sigma$ (white solid), $+3\sigma$ (white dashed), and -3σ (red dashed) contours. The lower subpanel shows the Stokes V image, overlaid with the Stokes I $+10\sigma$ (black solid) contour. The synthesized beam is shown in the lower-left corner.

Figure 3(b). The orbital parameters and geometric configuration of the FF UMa binary system, along with the corresponding spatial rotation diagram, are presented in Appendix B. In Figure 3(b), the green data points in the quiescent state are relatively close to the secondary star. Excluding the flaring epoch (epoch 6), the remaining five epochs show $\Delta\phi$ values ranging from $-60°$ to $+60°$, with a mean $\Delta\phi$ of $12\overset{\circ}{.}8 \pm 15\overset{\circ}{.}0$, and the mean separation is $\Delta R = 13.44 \pm 3.08\,R_\odot$.

4. Discussion

4.1. Evidence of Sustained Gyrosynchrotron Emission in the Quiescent State

Gyrosynchrotron emission is the major mechanism to explain high-frequency radio emission in a few radio-loud RS CVn binaries (e.g., M. Güdel 2002; W. W. Golay et al. 2023). Here, there is also strong evidence for the existence of sustained gyrosynchrotron emission in FF UMa in the quiescent state. Our multiepoch observations show that it had significant radio emission with a fractional circular polarization up to 25% over a span of 3 yr (see Figure 2). Such moderate fractional circular polarization is not typical of coherent emission via the electron-cyclotron maser emission (ECME; e.g., O. B. Slee et al. 2008; S. E. B. Toet et al. 2021; H. K. Vedantham et al. 2022). We estimated the brightness temperature to be $>2.0 \times 10^7$ K. The derived values are listed in Column (9) of Table 3. In epochs 1, 4, and 6, the deconvolved angular sizes represent only upper limits; therefore, the derived brightness temperatures should be regarded as lower limits. The high brightness temperature and the moderate fractional circular polarization indicate that the emission at 4.8 GHz was dominated by gyrosynchrotron radiation from mildly relativistic electrons (G. A. Dulk 1985) in strong magnetic fields.

Under this interpretation, we infer characteristic magnetic field strengths in the radio-emitting region of FF UMa on the order of 40–160 G (see Appendix C for details of the estimation). This range is broadly consistent with magnetic

Table 3
Summary of VLBA Stokes *I* and *V* Imaging Results of FF UMa

Epoch Stokes	Peak (mJy beam^{-1})	Integrated (mJy)	R.A. (mas)	Decl. (mas)	$\theta_{\rm Maj}$ (mas)	$\theta_{\rm Min}$ (mas)	$\theta_{\rm PA}$ (deg)	$T_{\rm b}$ (10^7K)
(1)	(2)	(3)	(4)	(5)	(6)	(7)	(8)	(9)
1-*I*	1.59 ± 0.09	2.02 ± 0.13	0.0000 ± 0.03	0.0000 ± 0.04	$1.8^{+0.3}_{-0.3}$	<0.7	⋯	>8.5
1-*V*	−0.33 ± 0.04	−0.54 ± 0.08	0.0555 ± 0.15	−0.2360 ± 0.19	<3.9	<1.2	⋯	⋯
2-*I*	1.73 ± 0.10	2.62 ± 0.17	0.0000 ± 0.01	0.0000 ± 0.04	$1.7^{+0.3}_{-0.2}$	$1.3^{+0.4}_{-0.5}$	49.8	6.2
2-*V*	−0.41 ± 0.04	−0.55 ± 0.07	−0.1125 ± 0.01	−0.0380 ± 0.11	<2.6	<1.8	⋯	⋯
3-*I*	5.97 ± 0.33	10.94 ± 0.67	0.0000 ± 0.05	0.0000 ± 0.03	$1.7^{+0.1}_{-0.1}$	$0.9^{+0.2}_{-0.6}$	93.9	37.9
3-*V*	±0.10	±0.10	⋯	⋯	⋯	⋯	⋯	⋯
4-*I*	0.88 ± 0.06	1.94 ± 0.15	0.0000 ± 0.09	0.0000 ± 0.06	<2.5	<2.1	⋯	>2.0
4-*V*	−0.12 ± 0.03	−0.42 ± 0.14	0.6120 ± 0.57	−0.5470 ± 0.59	<6.5	<2.9	⋯	⋯
5-*I*	1.81 ± 0.10	3.07 ± 0.17	0.0000 ± 0.03	0.0000 ± 0.02	$1.6^{+0.1}_{-0.1}$	$0.9^{+0.2}_{-0.3}$	46.8	11.3
5-*V*	−0.28 ± 0.03	−0.32 ± 0.06	0.8940 ± 0.13	0.1640 ± 0.12	<1.4	<1.8	⋯	⋯
6-*I*	18.78 ± 1.00	33.37 ± 1.90	0.0000 ± 0.04	0.0000 ± 0.02	<1.9	<1.9	⋯	>48.9
6-*V*	−0.48 ± 0.06	−0.76 ± 0.12	1.3305 ± 0.12	0.1830 ± 0.19	<4.2	<0.6	⋯	⋯
7-*I*	0.85 ± 0.05	1.79 ± 0.13	0.0000 ± 0.08	0.0000 ± 0.05	$2.0^{+0.2}_{-0.1}$	$1.3^{+0.3}_{-0.5}$	80.8	3.7
7-*V*	−0.20 ± 0.03	−0.32 ± 0.07	−0.9045 ± 0.26	−0.0500 ± 0.19	<2.8	<2.3	⋯	⋯

Note. All parameters listed in this table were derived using the AIPS task JMFIT. For the flux density measurements in Columns (2) and (3), the total uncertainties were obtained by combining the formal errors with an additional 5% systematic uncertainty in quadrature. The relative positions of Stokes *V* emission listed in Columns (4) and (5) are measured with respect to the centroid of the Stokes *I* emission at each epoch, which is adopted as the reference origin. The absolute astrometric positions of Stokes *I* emission were reported by J. Zhang et al. (2026). Columns (6)–(8) give the deconvolved sizes of major and minor axes and position angle of the fitted elliptical Gaussian components. No Stokes *V* emission was detected above the 4σ level at epoch 3. We therefore report the corresponding Stokes *V* flux densities as 3σ limits in the table. Column (9) lists the brightness temperatures for each epoch or lower limits when the source was not fully resolved.

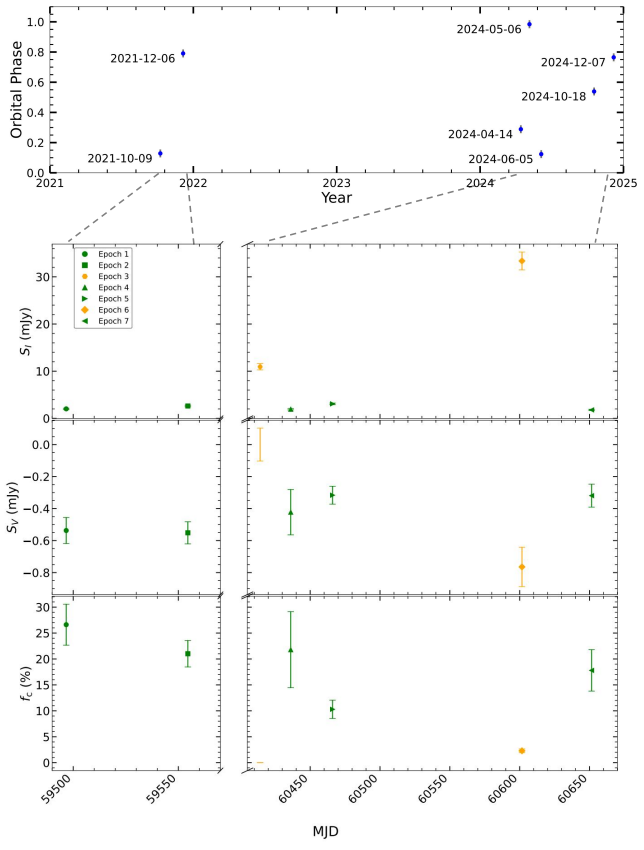

Figure 2. Top: orbital phase coverage of the multiepoch VLBA observations of FF UMa. The observing date and epoch number are labeled next to each point. Bottom: total intensity S_I (top), circularly polarized flux density S_V (middle), and fractional circular polarization f_c (bottom) versus observing time (MJD). Different marker shapes indicate different observing epochs. Green symbols denote quiescent states, while orange symbols mark flaring epochs.

field strengths reported for other RS CVn-type systems (e.g., F. N. Owen et al. 1976; S. R. Spangler 1977; D. M. Gibson et al. 1978; R. Estalella et al. 1993). The comparable levels of circular polarization further suggest that FF UMa, like other well-studied active binaries (e.g., R. L. Mutel & J. F. Lestrade 1985; R. L. Mutel et al. 1987; M. Massi et al. 1988), hosts large-scale, organized magnetic fields. Moreover, the sign of Stokes *V* traces the direction of the line-of-sight component of the magnetic field. The predominantly negative Stokes *V* detected in our observations therefore implies that the large-scale magnetic field in the radio-emitting region (e.g., extending to $\sim 40 R_\odot$ in epoch 7) maintains a systematic component directed away from the observer.

4.2. Anticorrelation between Circular Polarization Degree and Radio Luminosity

Figure 4 shows a significant decrease in fractional circular polarization with increasing radio luminosity ($L_{\rm R}$) in UX Ari, HR 1099, HR 5110 (R. L. Mutel et al. 1987; J. M. Paredes et al. 1987; R. Estalella et al. 1993), and our target FF UMa.

According to Q. Huang & B. Jiang (2025), the radio luminosity of RS CVn binaries depends on the orbital period. Using the radio flux densities reported in the sample of Q. Huang & B. Jiang (2025; gray points in Figure 4(a)), together with the radio flux densities of the four binary systems collected in this work (colored points in Figure 4(a)), we first fitted an empirical relation between the radio luminosity and the orbital period (P): $L_{\rm R} = 10^{15.88} P^{1.22}$. Based on this empirical relation, the radio luminosities of UX Ari, HR 1099, and HR 5110 were then rescaled to the orbital period of FF UMa. Figure 4(b) shows the resulting relation between the rescaled radio luminosity and the fractional circular polarization. Using uniform weighting, we fitted all the data and

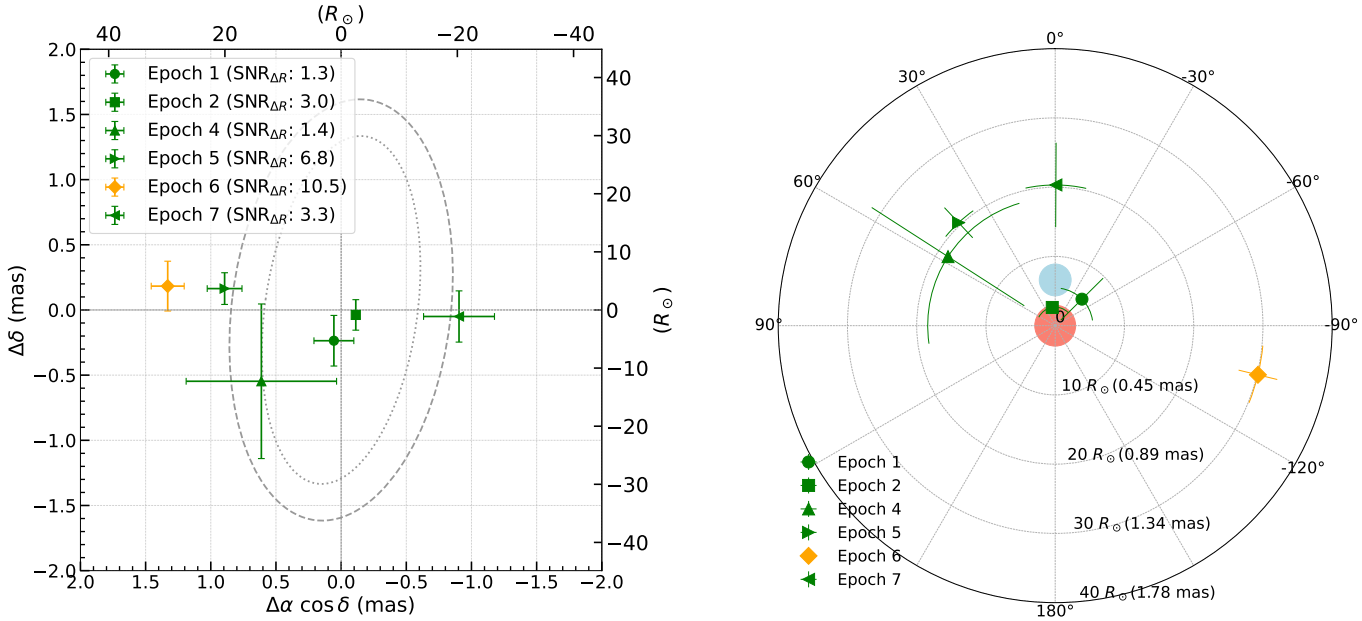

Figure 3. Positional offsets between the Stokes *I* and *V* centroids of FF UMa. Different symbols denoted different observing epochs. Epoch 6, which corresponded to a flaring state, was shown in orange, while the remaining epochs in quiescent states were shown in green. In both panels, the Stokes *I* position was taken as the coordinate origin and was not explicitly plotted. Left: offsets plotted in the sky plane. The SNR of the positional offset for each epoch was indicated in the legend. The gray dashed ellipses denote the synthesized beams with the minimum (Epoch 3) and maximum (Epoch 2) areas among all epochs. Right: offsets plotted in the binary reference frame. Red and blue circles indicate the positions of the primary and secondary stars, respectively; their sizes do not represent the actual physical scales of the stars, and 0° corresponds to the direction from the primary star toward the secondary star.

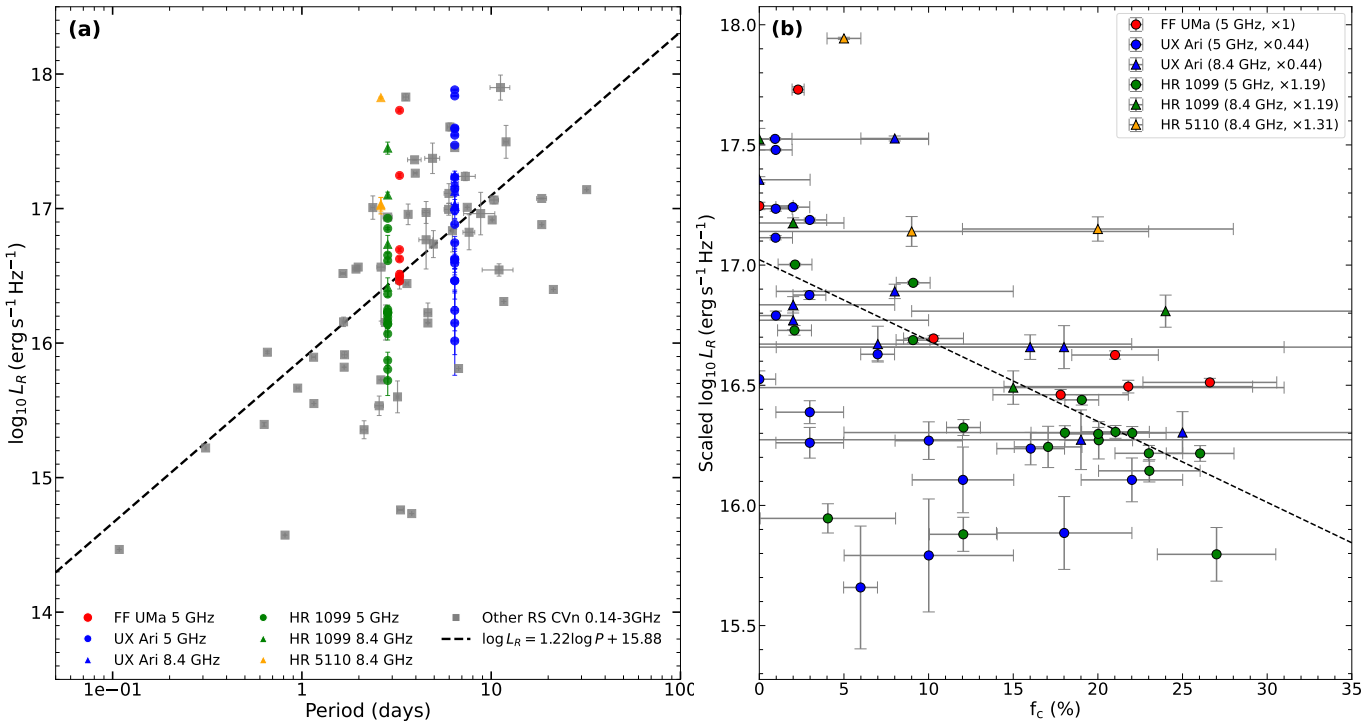

Figure 4. Left: relationship between radio luminosity and orbital period for RS CVn-type binary systems. The gray squares represent data from Q. Huang & B. Jiang (2025), including 42 RS CVn-type radio stars (FF UMa included), observed at frequencies between 144 and 3000 MHz. The shape of each symbol indicates the observing frequency: circles denote 5 GHz and triangles denote 8.4 GHz. Colors denote the sources: red for FF UMa, green for HR 1099, blue for UX Ari, and orange for HR 5110. The black dashed line shows the best-fitting relation obtained in this work. Right: relationship between the scaled radio luminosity and fractional circular polarization. The symbol colors and shapes are the same as in the left panel. The scaling factor applied to the radio luminosity of each source is indicated in the legend. The black dashed line represents the best-fitting relation derived in this work.

obtained the empirical relation

$$L_{\rm R} = 10^{-0.034 f_{\rm c} + 17.02}.$$

The dashed line in Figure 4(b) shows this fit.

The results discussed above indicate that FF UMa is as powerful as other well-characterized RS CVn binaries at radio wavelengths and follows a very similar anticorrelation trend. In the quiescent state, the radio emission is dominated by

gyrosynchrotron radiation. The anticorrelation may indicate that, in addition to the dominant gyrosynchrotron emission, synchrotron emission produced by relativistic electrons may also contribute to the radiation. Synchrotron radiation generally does not exhibit circular polarization; therefore, when this component becomes more prominent, the total radio luminosity can increase while the overall fractional circular polarization decreases. This scenario is consistent with our observations. During the two flaring epochs (epochs 3 and 6), the radio luminosity increases significantly, while the fractional circular polarization becomes much weaker or even undetectable. Nevertheless, gyrosynchrotron emission may still operate in some regions of the magnetosphere, indicating that the observed radio emission likely arises from multiple radiation mechanisms acting simultaneously. The large-scale magnetic field might also become poorly ordered because of various flares in the corona. In addition, flaring epoch 6 may have involved an internal eruption that displaced the radio-emitting region outward, which could account for the offset position of the yellow data point in Figure 3. A similar anticorrelation was also reported in other RS CVn systems in VLA studies (e.g., J. García-Sánchez et al. 2003).

4.3. Additional Gyrosynchrotron Emission from the Secondary Star?

The physical origin of the radio emission in RS CVn binary systems remains under debate. In FF UMa, the systematic spatial offset between the Stokes *I* and *V* emission centroids in Figure 3(b) supports a significantly nonuniform distribution of the degree of polarization. Assuming that the Stokes *I* emission is dominated by the primary star, the small offsets support the possibility that there exists a certain highly polarized emission associated with the secondary star (magnetic corona and loops), the interaction regions of magnetospheres (e.g., magnetopause), or both. The centroid position of Stokes *I* emission might also be linked to a giant magnetic loop on the surface of the primary star and thus have a large deviation ($\sim 10 R_{\odot}$) from the assumed reference position in Figure 3. Because of the limited image resolutions and astrometric precisions in our observations, it is hard to directly distinguish between these possible explanations. However, there is independent support for the presence of such large-scale magnetic structures on the surface of the secondary through Doppler imaging observations (H. V. Şenavcı et al. 2020), which reveal a semicircular distribution of starspots at latitudes of 10°–80°. To investigate these possible connections with the secondary, it would be necessary to carry out new VLBI observations at high frequencies in the future.

5. Conclusion

We reported multiepoch VLBA imaging results of the RS CVn binary system FF UMa at 5 GHz. In addition to total intensity emission, circularly polarized emission was firmly detected in six of seven epochs, with a maximum fractional circular polarization of 26%. The observed high brightness temperature ($\geqslant 10^7$ K) is also consistent with nonthermal gyrosynchrotron radiation from mildly relativistic electrons in the stellar magnetosphere. Our high-resolution studies provide strong evidence for long-lived luminous gyrosynchrotron radiation and highly ordered magnetic fields for the first time in FF UMa. Moreover, we noticed marginal spatial offsets between the Stokes *I* and *V* emission centroids, reflecting the inhomogeneous spatial distribution of the large-scale ordered magnetic field. These results tend to support the scenario that the magnetic corona and giant loops in the secondary and magnetic interactions within the binary system also influenced the observed radio emission and its polarization properties. Thus, FF UMa might be an ideal magnetic active binary for future high-resolution deep multi-epoch VLBI observations to explore the structure, interaction, and evolution of large-scale magnetic fields in RS CVn systems.

Acknowledgments

This research is supported by the National SKA Program of China (2022SKA0120101). Y.G. is supported by National Natural Science Foundation of China (NSFC) under grant No. 42150105. J.Z. is supported by the Postdoctoral Programme for Research Institutes in Finland funded by the Finnish Government. B.Z. is supported by the National Key R&D Program of China (No. 2024YFA1611501) and the Strategic Priority Research Program of the Chinese Academy of Sciences (No. XDA0350205). W.C. and B.Z. are supported by National Natural Science Foundation of China (NSFC) under grant No. 12573073, Yunnan Fundamental Research Projects (grant No. 202401AT070144), and Yunnan Foreign Talent Introduction Program (grant No. 202505AO120021). G.G. is supported by Yunnan Fundamental Research Projects (No. 202301AT070325). Z.D. is supported by the Yunnan Youth Talent Project and the Yunnan Fundamental Research Projects (grant No. 202201AT070180). The National Radio Astronomy Observatory (NRAO) is a facility of the National Science Foundation (NSF), operated under cooperative agreement by Associated Universities, Inc.

Appendix

This appendix provides some additional details including the calibrator images, the geometric configuration of the binary orbit, and the procedures that we used to calculate magnetic field strength.

Appendix A
Calibrator Images

Figure 5 shows the images of the phase calibrator J0921 +6215 in epoch 2. In all seven epochs, no Stokes *V* signal above 3σ was detected within the on-source region.

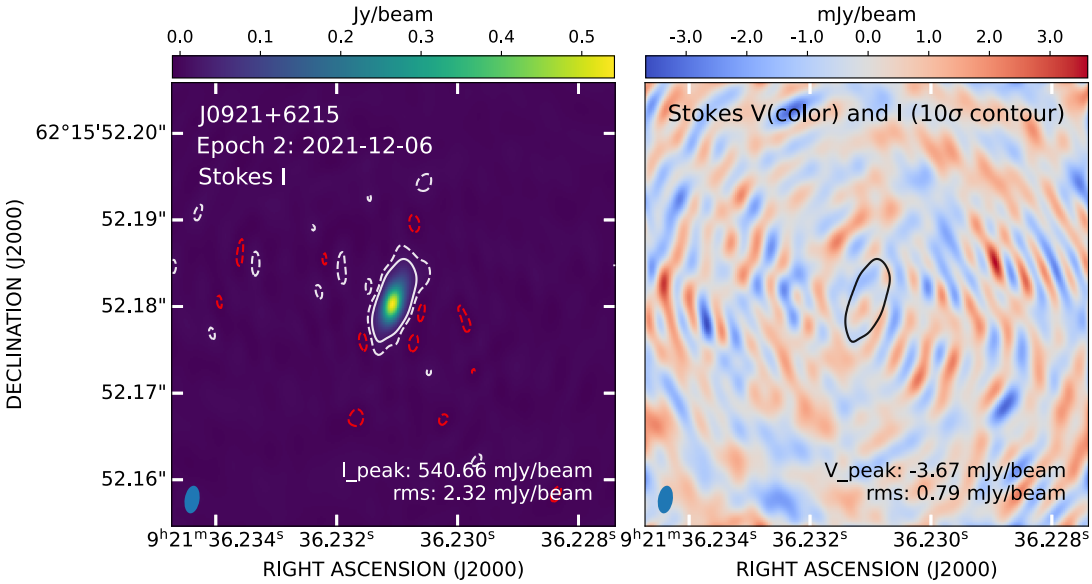

Figure 5. Calibrator J0921+6215 in epoch 2. Left: Stokes I image with its $+10\sigma$ (white solid), $+3\sigma$ (white dashed), and -3σ (red dashed) contours. Right: Stokes V image overlaid with the Stokes I $+10\sigma$ (black solid) contour.

Appendix B
The Geometric Relationships and Spatial Rotation Diagram of FF UMa

From past optical spectroscopic studies of FF UMa, several orbital elements of the binary system are known, such as the semimajor axis, orbital period, and eccentricity (see Table 1). Based on H. V. Şenavcı et al. (2020), and assuming the binary system rotates counterclockwise, its spatial projection on the sky plane is shown in Figure 6. The orbital positions shown correspond to phase 0. FF UMa is a nearly face-on binary system, and no eclipses occur along our line of sight.

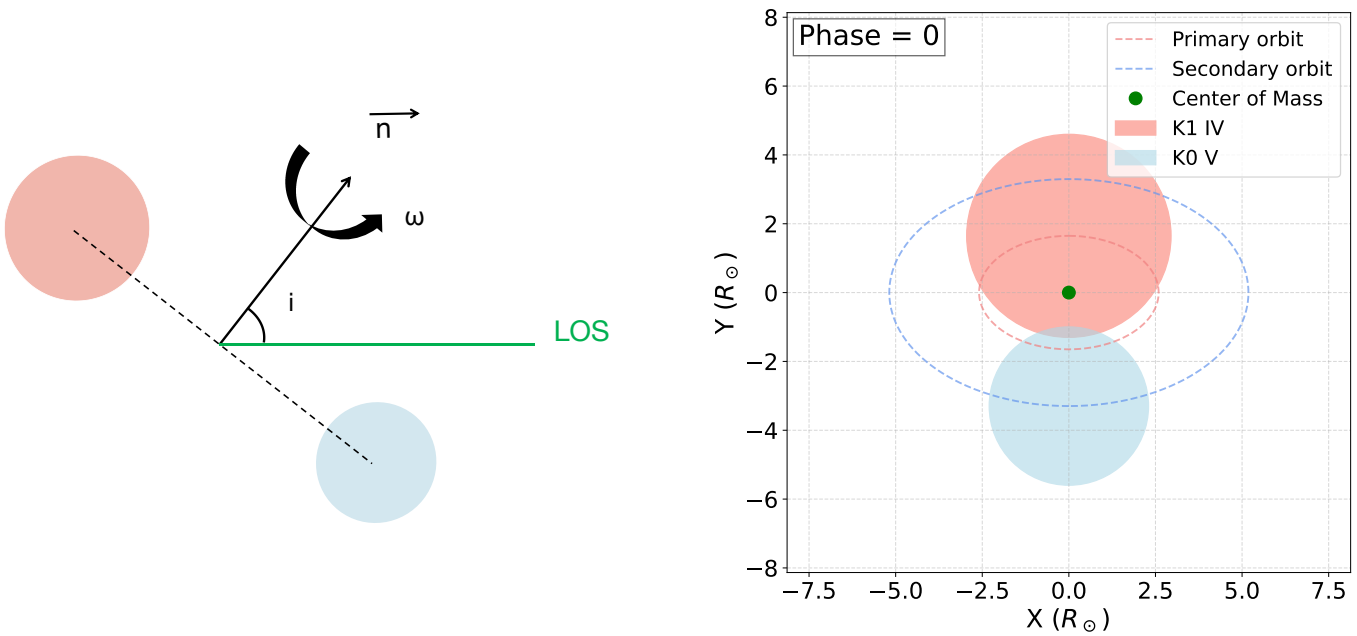

Figure 6. Binary positions of the FF UMa system at phase = 0, with red and blue circles representing the primary and secondary stars. Left: relative positions of the binary components. Stellar sizes and separations are schematic and do not represent true physical scales. The black dashed line indicates the orbital plane, the black straight arrow represents the orbital angular momentum vector (normal to the orbital plane), the black curved arrow shows the direction of orbital motion, and the green solid line indicates the line of sight. i denotes the orbital inclination, $i = 50.^{\circ}5$. Right: relative positions of the binary components projected onto the plane of the binary orbit. Physical parameters are consistent with those listed in Table 1. Red and blue dashed ellipses represent the orbital trajectories of the primary and secondary stars, respectively.

Appendix C
Magnetic Field Strength Calculation

Assuming a power-law energy distribution for the emitting electrons, the effective temperature of gyrosynchrotron emission can be written as (Equation (37) G. A. Dulk 1985)

$$T_{\rm eff} \approx 2.2 \times 10^9 10^{-0.31\delta} (\sin\theta)^{-0.36-0.06\delta} \times \left(\frac{\nu}{\nu_{\rm B}}\right)^{0.50+0.085\delta}, \quad \text{(C1)}$$

where δ is the electron energy spectral index, θ is the angle between the line of sight and the magnetic field direction, ν is the observing frequency in GHz, and $\nu_{\rm B}$ is the electron gyrofrequency,

$$\nu_{\rm B} = \frac{eB}{2\pi m_e} \approx 2.80 \times 10^{-3} B \quad \text{(C2)}$$

with B in Gauss.

For active stellar coronae, the electron energy spectral index is typically found in the range $\delta \simeq 3$–5 (e.g., G. A. Dulk 1985). In addition, the viewing angle θ between the magnetic field and the line of sight is generally unconstrained observationally; therefore, we explore a representative range of $\theta = 20°$, 40°, and 60°.

The above approximation is valid for $10 < \nu/\nu_{\rm B} < 100$. For each combination of δ and θ within the above ranges that satisfies this condition, we estimate the corresponding magnetic field strength by equating $T_{\rm eff}$ to the observed brightness temperature. This yields characteristic magnetic field strengths in the range $B \simeq 40$–160 G.

The corresponding electron gyrofrequencies are $\nu_{\rm B} \sim 0.1$–0.45 GHz. We suggest that, at frequencies comparable to or below the electron gyrofrequency, coherent ECME may become important and possibly dominate, typically producing very high fractional circular polarization (>50%). Indeed, H. K. Vedantham et al. (2022) reported highly circularly polarized emission from FF UMa at 0.144 GHz with a fractional circular polarization as high as 74% in right-hand circular polarization, consistent with this interpretation.

The VLBA observations analyzed here primarily probe the quiescent radio emission of FF UMa. Significant gyrosynchrotron emission from thermal electrons would require coronal temperatures of order $\sim 10^8$ K, which are typically reached only during strong radio or X-ray flares (W. W. Golay et al. 2023; J. Wang et al. 2026). There is no evidence that our VLBA observations correspond to such flaring states. Under quiescent conditions, any contribution from thermal electrons is therefore expected to be negligible.

ORCID iDs

Ruijie Gao https://orcid.org/0009-0003-1870-5164
Jun Yang https://orcid.org/0000-0002-2322-5232
Yang Gao https://orcid.org/0000-0002-6316-1632
Jingdong Zhang https://orcid.org/0000-0002-9768-2700
Bo Zhang https://orcid.org/0000-0003-1353-9040
Wen Chen https://orcid.org/0000-0002-5519-0628
Xiaohui Sun https://orcid.org/0000-0002-3464-5128
Guannan Gao https://orcid.org/0000-0001-6383-6751
Zhibin Dai https://orcid.org/0000-0002-4280-6630
Tobia D. Carozzi https://orcid.org/0000-0002-4963-179X

References

Abbuhl, E., Mutel, R. L., Lynch, C., & Güedel, M. 2015, ApJ, 811, 33
Ayres, T. R., & Linsky, J. L. 1980, ApJ, 241, 279
Becker, R. H., White, R. L., & Helfand, D. J. 1995, ApJ, 450, 559
Brun, A. S., & Browning, M. K. 2017, LRSP, 14, 4
Chen, W., & Wang, M. 2023, AstTI, 20, 412
Chen, W., Zhang, B., Zhang, J., et al. 2023, MNRAS, 524, 5357
Condon, J. J., Cotton, W. D., Greisen, E. W., et al. 1998, AJ, 115, 1693
Deller, A. T., Tingay, S. J., Bailes, M., & West, C. 2007, PASP, 119, 318
Drake, S. A., Simon, T., & Linsky, J. L. 1989, ApJS, 71, 905
Dulk, G. A. 1985, ARA&A, 23, 169
Estalella, R., Paredes, J. M., Rius, A., Marti, J., & Peracaula, M. 1993, A&A, 268, 178
Gálvez, M. C., Montes, D., Fernández-Figueroa, M. J., de Castro, E., & Cornide, M. 2007, A&A, 472, 587
García-Sánchez, J., Paredes, J. M., & Ribó, M. 2003, A&A, 403, 613
Gibson, D. M., Hicks, P. D., & Owen, F. N. 1978, AJ, 83, 1495
Golay, W. W., Mutel, R. L., & Abbuhl, E. E. 2024, ApJ, 965, 86
Golay, W. W., Mutel, R. L., Lipman, D., & Güdel, M. 2023, MNRAS, 522, 1394
Greisen, E. W. 2003, ASSL, 285, 109
Griffin, R. F. 2012, A&A, 537, A56
Güdel, M. 2002, ARA&A, 40, 217
Hall, D. S. 1981, ASSL, 60, 287
Homan, D. C., & Lister, M. L. 2006, AJ, 131, 1262
Homan, D. C., & Wardle, J. F. C. 1999, AJ, 118, 1942
Huang, Q., & Jiang, B. 2025, ApJ, 992, 97
Jeffries, R. D., Bertram, D., & Spurgeon, B. R. 1995, MNRAS, 276, 397
Lacy, M., Baum, S. A., Chandler, C. J., et al. 2020, PASP, 132, 035001
Lestrade, J. F., Mutel, R. L., Phillips, R. B., et al. 1984, ApJL, 282, L23
Massi, M., Felli, M., Pallavicini, R., et al. 1988, A&A, 197, 200
Matthews, L. D. 2025, PASP, 137, 116001
Morris, D. H., & Mutel, R. L. 1988, AJ, 95, 204
Murphy, T., & Kaplan, D. L. 2026, PASA, 43, e006
Mutel, R. L., Doiron, D. J., Lestrade, J. F., & Phillips, R. B. 1984, ApJ, 278, 220
Mutel, R. L., & Lestrade, J. F. 1985, AJ, 90, 493
Mutel, R. L., Lestrade, J. F., Preston, R. A., & Phillips, R. B. 1985, ApJ, 289, 262
Mutel, R. L., Morris, D. H., Doiron, D. J., & Lestrade, J. F. 1987, AJ, 93, 1220
Owen, F. N., Jones, T. W., & Gibson, D. M. 1976, ApJL, 210, L27
Paredes, J. M., Estalella, R., & Rius, A. 1987, A&A, 186, 177
Peterson, W. M., Mutel, R. L., Lestrade, J.-F., Güdel, M., & Goss, W. M. 2011, ApJ, 737, 104
Phillips, R. B., Lonsdale, C. J., Feigelson, E. D., & Deeney, B. D. 1996, AJ, 111, 918
Pounds, K. A., Allan, D. J., Barber, C., et al. 1993, MNRAS, 260, 77
Ransom, R. R., Bartel, N., Bietenholz, M. F., et al. 2002, ApJ, 572, 487
Rioja, M. J., Dodson, R., Orosz, G., Imai, H., & Frey, S. 2017, AJ, 153, 105
Salter, D. M., Kóspál, Á., Getman, K. V., et al. 2010, A&A, 521, A32
Şenavcı, H. V., Bahar, E., Özavcı, İ., & Kılıçoğlu, T. 2020, CoSka, 50, 594
Shimwell, T. W., Röttgering, H. J. A., Best, P. N., et al. 2017, A&A, 598, A104
Slee, O. B., Wilson, W., & Ramsay, G. 2008, PASA, 25, 94
Spangler, S. R. 1977, AJ, 82, 169
Strassmeier, K., Washuettl, A., Granzer, T., Scheck, M., & Weber, M. 2000, A&AS, 142, 275
Strassmeier, K. G., Weber, M., Granzer, T., & Järvinen, S. 2012, AN, 333, 663
Toet, S. E. B., Vedantham, H. K., Callingham, J. R., et al. 2021, A&A, 654, A21
Vedantham, H. K., Callingham, J. R., Shimwell, T. W., et al. 2022, ApJL, 926, L30
Wang, J., Xie, W. J., Cangemi, F., et al. 2026, ApJ, 998, 287
Zhang, J., Zhang, B., Xu, S., & Mai, X. 2025, A&A, 699, A345
Zhang, J., Zhang, B., Xu, S., et al. 2024, MNRAS, 529, 2062
Zhang, J., Zhang, B., Xu, S., et al. 2026, MNRAS, 547, stag244